The Astrophysical Journal, 925:16 (12pp), 2022 January 20 https://doi.org/10.3847/1538-4357/ac3996

Effects of the ϕ Meson on the Properties of Hyperon Stars in the Density-dependent Relativistic Mean Field Model

Zhong-Hao Tu[1,2] and Shan-Gui Zhou[1,2,3,4]
[1] CAS Key Laboratory of Theoretical Physics, Institute of Theoretical Physics, Chinese Academy of Sciences, Beijing, 100190, People's Republic of China
sgzhou@itp.ac.cn
[2] School of Physical Sciences, University of Chinese Academy of Sciences, Beijing, 100049, People's Republic of China
[3] Center of Theoretical Nuclear Physics, National Laboratory of Heavy Ion Accelerator, Lanzhou, 730000, People's Republic of China
[4] Synergetic Innovation Center for Quantum Effects and Application, Hunan Normal University, Changsha, 410081, People's Republic of China
Received 2021 September 13; revised 2021 November 3; accepted 2021 November 10; published 2022 January 21

Abstract

The effects of the ϕ meson on the properties of hyperon stars are studied systematically in the framework of the density-dependent relativistic mean field (DDRMF) model. The ϕ meson shifts the hyperon threshold to a higher density and reduces the hyperon fractions in neutron star cores. It also strongly stiffens the equation of state calculated with various DDRMF effective interactions and increases the maximum mass of hyperon stars, but only a few effective interactions survive under the constraints from recent astrophysical observations. In the DDRMF model, the conformal limit of the sound velocity is still in strong tension with the fact that the maximum mass of neutron stars obtained in theoretical calculations reaches about 2 $M_\odot$. Based on different interior composition assumptions, we discuss the possibility of the secondary object of GW190814 as a neutron star. When the ϕ meson is considered, DD-ME2 and DD-MEX support the possibility that the secondary object of GW190814 is a hyperon star rapidly rotating with Kepler frequency.

Key words: Neutron stars – Nuclear astrophysics – Neutron star cores – Compact objects

1. Introduction

Neutron stars provide an ideal laboratory to probe the physical mechanism of dense matter at baryon number density ρ_B above twice the nuclear saturation density ρ_0 and isospin asymmetry close to pure neutron matter. The interior composition and equation of state (EoS) of neutron star cores ($\rho_B \gtrsim 2\rho_0$) are still little known. Based on different theoretical assumptions, a number of possibilities have been proposed for the composition of the inner core, such as nucleons (Li et al. 2016; Zhu et al. 2018; Zhu & Li 2018; Zhu et al. 2019), nucleons mixed with excited nucleons (Δ; Xiang & Hua 2003; Drago et al. 2014; Zhu et al. 2016; Li et al. 2018; Sun et al. 2019; Thapa et al. 2021a, 2021b), strange meson condensation (Schaffner & Mishustin 1996; Li et al. 2006, 2007, 2010; Lim et al. 2014; Thapa & Sinha 2020; Thapa et al. 2021b), deconfined quarks (hybrid stars and quark stars; Alford et al. 2013; Shao et al. 2013; Xia et al. 2016a, 2016b; Wei et al. 2017; Maslov et al. 2019), and hyperons (hyperon stars; Glendenning 1985; Schaffner & Mishustin 1996; Li et al. 2007; Weissenborn et al. 2012a; Katayama & Saito 2015; Oertel et al. 2015; Hong et al. 2019; Providência et al. 2019; Rather et al. 2021a; Thapa et al. 2021b). The different composition assumptions of neutron star cores lead to large uncertainties in the EoSs of neutron stars. Exploring the interior composition and constraining the EoS require combining astrophysics and nuclear physics.

Several neutron stars with about 2 $M_\odot$, including PSR J1614–2230 with 1.908 ± 0.016 $M_\odot$ (Demorest et al. 2010), PSR J0348+0432 with 2.01 ± 0.04 $M_\odot$ (Antoniadis et al. 2013), and MSP J0740+6620 with $2.08^{+0.07}_{-0.07} M_\odot$ (Fonseca et al. 2021), put a strong constraint on the maximum mass of neutron stars calculated with theoretical approaches. The first gravitational-wave (GW) signal from GW170817 of a binary neutron star (BNS) merger was observed by the LIGO Scientific Collaboration and Virgo Collaboration (Abbott et al. 2017), and the constraints from the GW signal on the EoS and neutron star radius were performed in Abbott et al. (2018). The observation of GW170817 opened up a new era of multi-messenger astronomy. The Neutron star Interior Composition Explorer (NICER) has been devoted to the study of the internal structure of neutron stars by soft X-ray timing (Gendreau & Arzoumanian 2017), and a large number of studies have been performed to constrain the EoS and mass–radius relation of neutron stars (Bogdanov et al. 2019a, 2019b; Miller et al. 2019; Jiang et al. 2020; Raaijmakers et al. 2020). The advanced astronomical observation techniques will provide more information about neutron stars and help us to investigate the interior compositions of neutron stars and the behaviors of EoSs of dense matter at extreme densities.

Various theoretical approaches have been used to study the properties of homogeneous nuclear matter, including ab initio (Zuo et al. 2002a, 2002b; Baldo & Maieron 2004; Dickhoff & Barbieri 2004; Bombaci et al. 2005; Lee 2009; Baldo et al. 2012; Carlson et al. 2015) and phenomenological (Glendenning 1985; Rikovska Stone et al. 2003; Stone & Reinhard 2007; Dutra et al. 2012, 2014; Sellahewa & Rios 2014; Whittenbury et al. 2014) approaches, and these studies cover large ranges of baryon number density, temperature, and isospin asymmetry. The relativistic mean field (RMF) model, one of the phenomenological models, provides an excellent tool to study the properties of infinite nuclear matter (Chin & Walecka 1974; Walecka 1974; Glendenning 1996; Shen & Ren 1999; Shen 2002; Shen et al. 2011; Zhao & Jia 2012; Dutra et al. 2014; Zhao 2014; Meng et al. 2016; Bhuyan et al. 2017; Mu et al. 2017; Biswal et al. 2019; Tong et al. 2020). In the framework of the RMF model, the baryons are treated as point

particles and interact with each other through the exchange of scalar and vector mesons (Walecka 1974; Glendenning 1985). The coupling constants between nucleons and mesons are determined by fitting nuclear matter properties and/or the properties of selected finite nuclei (Schaffner & Mishustin 1996). Using different parameterization strategies, like nonlinear (NL) and density-dependent (DD), the EoSs of nuclear matter with different stiffness are obtained at high density even though they are constrained well at saturation density. An RMF effective interaction may be excluded if its predictions are incompatible with astrophysical observations.

As we mentioned above, various hyperons may be populated in the inner core of neutron stars at a density of about 2–3ρ_0 once the nucleon Fermi energy reaches the (in-medium) rest masses of the hyperons (Glendenning 1985). However, the appearance of hyperons results in the *hyperon puzzle*; hyperons strongly soften the EoS so that the maximum mass is not compatible with observations (Schulze et al. 2006; Vidaña 2013). The solution of the hyperon puzzle requires additional repulsive interaction between baryons (Vidaña 2013), and mechanisms that provide such repulsion include (a) addition of the repulsive hyperonic three-body force (Lonardoni et al. 2015; Wirth & Roth 2016), (b) a deconfinement phase transition to quark matter below the hyperon thresholds (Weissenborn et al. 2011; Bonanno & Sedrakian 2012; Klähn et al. 2013), and (c) addition of the repulsive hyperonic interaction by exchanging vector meson (Weissenborn et al. 2012a; Maslov et al. 2015; Bhuyan et al. 2017). In the framework of the RMF model, the additional repulsive interaction between hyperons can be achieved by including the strange meson ϕ (Schaffner & Mishustin 1996; Weissenborn et al. 2013; Zhao 2015; Fortin et al. 2017; Tolos et al. 2017; Lopes & Menezes 2021).

The effects of the ϕ meson on the properties of neutron stars have been studied in the NLRMF model (Weissenborn et al. 2012b; Banik et al. 2014; Biswal et al. 2019; Lopes & Menezes 2020). But in the density-dependent relativistic mean field (DDRMF) model, the effects of the ϕ meson on the interior composition, EoS, sound velocity, and mass–radius relation of neutron stars are still missing. In the present work, combining with the widely used effective interactions DD-ME2 (Lalazissis et al. 2005), DD-MEδ (Roca-Maza et al. 2011), PKDD (Long et al. 2004), and TW99 (Typel & Wolter 1999) and the latest proposed effective interactions DD-MEX (Taninah et al. 2020), DDV, DDVT, and DDVTD (Typel & Terrero 2020), we systematically study the effects of the ϕ meson on the properties of hyperon stars in the framework of the DDRMF model. The recent astrophysical observations, e.g., MSP J0740+6620 and the GW190814 event, are used to discuss the significance of the ϕ meson on hyperon stars. For studying the effects of the ϕ meson alone, the other strange meson, σ^*, whose properties are little known, is neglected in this work.

This paper is organized as follows. In Section 2, the theoretical framework of the DDRMF model and the methodology for calculating the mass–radius relations of neutron stars are given. In Section 3, we present the results and discussions of the interior composition, EoS, sound velocity, and mass–radius relation of neutron stars. Finally, a brief summary is given in Section 4.

2. Theoretical Framework

Since the Walecka model was proposed (Walecka 1974), the RMF approach has been extended to the NLRMF and DDRMF models in order to simulate the medium-dependent effective interaction (Boguta & Bodmer 1977; Reinhard 1989; Fuchs et al. 1995), and both have been successfully applied to the study of nuclear matter and finite nuclei (Reinhard 1989; Ring 1996; Bender et al. 2003; Meng et al. 2006; Nikšić et al. 2011; Meng & Zhou 2015; Oertel et al. 2017). Unlike the NLRMF model, the coupling constants between baryons and mesons in the DDRMF model are DD. In the present work, we focus on the DDRMF model and consider all octet baryons (n, p, Λ, Σ^+, Σ^0, Σ^-, Ξ^0, and Ξ^-) and isoscalar mesons (σ and ω), isovector mesons (ρ and δ), and the hidden-strangeness vector meson ϕ. For convenience, we use the $npe\mu$ matter to represent the nuclear matter that consists of nucleons, leptons, and nonstrangeness mesons. If hyperons are included as well, we call it the $npe\mu Y$ matter. In the $npe\mu Y\phi$ matter, the ϕ meson effects are taken into account. The corresponding neutron stars are labeled as $npe\mu$, $npe\mu Y$, and $npe\mu Y\phi$ neutron stars, respectively. The general Lagrangian of the DDRMF model that describes the infinite nuclear matter of neutron star cores can be written as

$$\begin{aligned}\mathcal{L} = & \textstyle\sum_B \bar{\psi}_B\{\gamma^\mu[i\partial_\mu - \Gamma_{\omega B}(\rho_B)\omega_\mu \\ & - \Gamma_{\rho B}(\rho_B)\boldsymbol{\rho}_\mu\boldsymbol{\tau}_B - \Gamma_{\phi B}(\rho_B)\phi_\mu] \\ & - [M_B + \Gamma_{\sigma B}(\rho_B)\sigma + \Gamma_{\delta B}(\rho_B)\boldsymbol{\delta}\boldsymbol{\tau}_B]\}\psi_B \\ & + \frac{1}{2}(\partial^\mu\sigma\partial_\mu\sigma - m_\sigma^2\sigma^2) + \frac{1}{2}(\partial^\mu\boldsymbol{\delta}\partial_\mu\boldsymbol{\delta} - m_\delta^2\boldsymbol{\delta}^2) \\ & - \frac{1}{4}W^{\mu\nu}W_{\mu\nu} + \frac{1}{2}m_\omega^2\omega^\mu\omega_\mu - \frac{1}{4}\boldsymbol{R}^{\mu\nu}\boldsymbol{R}_{\mu\nu} \\ & + \frac{1}{2}m_\rho^2\boldsymbol{\rho}^\mu\boldsymbol{\rho}_\mu - \frac{1}{4}\Phi^{\mu\nu}\Phi_{\mu\nu} + \frac{1}{2}m_\phi^2\phi^\mu\phi_\mu \\ & + \textstyle\sum_l \bar{\psi}_l(i\gamma_\mu\partial^\mu - m_l)\psi_l, \end{aligned} \tag{1}$$

where $\boldsymbol{\tau}_B$ is the Pauli matrices for the isospin of the baryon species B; M_B and m_l represent the baryon and lepton masses, respectively; $\psi_{B(l)}$ is the Dirac field of the baryon species B or the lepton species l; and σ, ω_μ, $\boldsymbol{\rho}_\mu$, $\boldsymbol{\delta}$, and ϕ_μ denote the quantum fields of mesons. The antisymmetric field strength tensors ($W_{\mu\nu}$, $\boldsymbol{R}_{\mu\nu}$, and $\Phi_{\mu\nu}$) of the vector mesons (ω, ρ, and ϕ) are

$$\begin{aligned} W_{\mu\nu} &= \partial_\mu\omega_\nu - \partial_\nu\omega_\mu, \\ \boldsymbol{R}_{\mu\nu} &= \partial_\mu\vec{\rho}_\nu - \partial_\nu\vec{\rho}_\mu, \\ \Phi_{\mu\nu} &= \partial_\mu\phi_\nu - \partial_\nu\phi_\mu. \end{aligned} \tag{2}$$

Under the mean field approximation, all quantum fluctuations of meson fields are neglected, and the meson fields are treated as classical fields. Then, the equations of motion of various mesons are obtained via the Euler–Lagrange equation,

$$\begin{aligned} m_\sigma^2\sigma &= -\textstyle\sum_B \Gamma_{\sigma B}(\rho_B)\rho_s^B, \\ m_\omega^2\omega &= \textstyle\sum_B \Gamma_{\omega B}(\rho_B)\rho_v^B, \\ m_\rho^2\rho &= \textstyle\sum_B \Gamma_{\rho B}(\rho_B)\rho_v^B\tau_B^3, \\ m_\delta^2\delta &= -\textstyle\sum_B \Gamma_{\delta B}(\rho_B)\rho_s^B\tau_B^3, \\ m_\phi^2\phi &= \textstyle\sum_B \Gamma_{\phi B}(\rho_B)\rho_v^B, \end{aligned} \tag{3}$$

where τ_B^3 is the isospin projection of the baryon species B. The vector density ρ_v^B and scalar density ρ_s^B of the baryon species B read

$$\rho_v^B = \frac{1}{\pi^2}\int_0^{k_F^B} k^2 \mathrm{d}k = \frac{(k_F^B)^3}{3\pi^2},$$
$$\rho_s^B = \frac{M_B^\star}{\pi^2}\int_0^{k_F^B} \frac{k^2 \mathrm{d}k}{\sqrt{k^2 + M_B^{\star 2}}} = \frac{(M_B^\star)^3}{2\pi^2} \times [q\sqrt{1+q^2} - \ln(q+\sqrt{1+q^2})], \quad q = \frac{k_F^B}{M_B^\star}, \tag{4}$$

with the Fermi momentum k_F^B and effective mass $M_B^\star = M_B + \Gamma_{\sigma B}(\rho_B)\sigma + \Gamma_{\delta B}(\rho_B)\delta\tau_B^3$ of the baryon species B.

Inside the neutron star cores, the baryon and lepton compositions satisfy the β-equilibrium conditions

$$\mu_n - q_B\mu_e = \mu_B,$$
$$\mu_\mu = \mu_e, \tag{5}$$

where q_B is the charge of the baryon species B. Here μ_B (μ_l), which stands for the chemical potential of the baryon species B (lepton species l), is given by

$$\mu_B(k_F^B) = \sqrt{(k_F^B)^2 + M_B^{\star 2}} + \Gamma_{\omega B}(\rho_B)\omega + \Gamma_{\rho B}(\rho_B)\rho\tau_3^B + \Gamma_{\phi B}(\rho_B)\phi + \Sigma_R,$$
$$\mu_l(k_F^l) = \sqrt{(k_F^l)^2 + M_l^{\star 2}}. \tag{6}$$

The density dependence of the coupling constants between baryons and mesons leads to the rearrangement term Σ_R in Equation (6) (Fuchs et al. 1995),

$$\Sigma_R = \sum_B \left[-\frac{\partial\Gamma_{\sigma B}(\rho_B)}{\partial\rho_B}\sigma\rho_s^B - \frac{\partial\Gamma_{\omega B}(\rho_B)}{\partial\rho_B}\omega\rho_v^B - \frac{\partial\Gamma_{\rho B}(\rho_B)}{\partial\rho_B}\rho\rho_v^B\tau_3^B - \frac{\partial\Gamma_{\delta B}(\rho_B)}{\partial\rho_B}\delta\rho_s^B\tau_3^B - \frac{\partial\Gamma_{\phi B}(\rho_B)}{\partial\rho_B}\phi\rho_v^B \right]. \tag{7}$$

Several different forms have been proposed for the density dependence of the coupling constants (de Jong & Lenske 1998; Typel & Wolter 1999). For all effective interactions we use in this work, the coupling constants between baryons and isoscalar mesons (σ and ω) are given by

$$\Gamma_{iB}(x) = \Gamma_{iB}(\rho_0)a_i\frac{1 + b_i(x+d_i)^2}{1 + c_i(x+e_i)^2}, \quad x = \rho_B/\rho_0. \tag{8}$$

For the coupling constants between baryons and isovector mesons (ρ and δ), the density dependence in DD-MEδ takes the form of Equation (8), but in other effective interactions, it reads

$$\Gamma_{iB}(x) = \Gamma_{iB}(\rho_0)^{-a_i(x-1)}, \ x = \rho_B/\rho_0. \tag{9}$$

For the coupling constants between hyperons and mesons, we apply the relations from the SU(6) naive quark model for ω, ρ, δ, and ϕ (Schaffner & Mishustin 1996; Shao & Liu 2010):

$$\Gamma_{\omega\Lambda} = \Gamma_{\omega\Sigma} = 2\Gamma_{\omega\Xi} = \frac{2}{3}\Gamma_{\omega N},$$
$$\Gamma_{\rho\Lambda} = 0, \ \Gamma_{\rho\Sigma} = 2\Gamma_{\omega\Xi} = 2\Gamma_{\omega N},$$
$$\Gamma_{\delta\Lambda} = 0, \ \Gamma_{\delta\Sigma} = 2\Gamma_{\delta\Xi} = 2\Gamma_{\delta N},$$
$$\Gamma_{\phi N} = 0, \ 2\Gamma_{\phi\Lambda} = 2\Gamma_{\phi\Sigma} = \Gamma_{\phi\Xi} = -\frac{2\sqrt{2}}{3}\Gamma_{\omega N}. \tag{10}$$

As for the σ meson, we determine the coupling constants between hyperons and σ by fitting empirical hypernuclear potentials using the following formula:

$$U_Y^{(N)} = R_{\sigma Y}\Gamma_{\sigma N}^0\sigma^0 + R_{\omega Y}\Gamma_{\omega N}^0\omega^0 + \Sigma_R^0, \tag{11}$$

where $\Gamma_{\sigma N}^0$, $\Gamma_{\omega N}^0$, σ^0, ω^0, and Σ_R^0 are the values of the symmetric nuclear matter at the saturation density, and $R_{\sigma Y}$ ($R_{\omega Y}$) is the ratio of $\Gamma_{\sigma Y}$ to $\Gamma_{\sigma N}$ ($\Gamma_{\omega Y}$ to $\Gamma_{\omega N}$). We choose $U_\Lambda^{(N)} = -30$ MeV (Schaffner-Bielich & Gal 2000; Wang & Shen 2010), $U_\Sigma^{(N)} = +30$ MeV, and $U_\Xi^{(N)} = -15$ MeV (Ishizuka et al. 2008; Wang & Shen 2010) in the present work.

The charge neutrality condition $\rho_v^p + \rho_v^{\Sigma^+} = \rho_v^e + \rho_v^\mu + \rho_v^{\Sigma^-} + \rho_v^{\Xi^-}$ and baryon number conservation condition $\rho_B = \sum_B \rho_v^B$ are satisfied inside neutron star cores. With these two conditions, we can obtain the meson fields and Fermi momenta of baryons and leptons by solving the NL coupled Equations (3) and (5) self-consistently at a given baryon number density. Furthermore, the energy density ε and pressure P can be calculated by using the energy–momentum tensor,

$$\varepsilon = \frac{1}{2}m_\sigma^2\sigma^2 + \frac{1}{2}m_\omega^2\omega^2 + \frac{1}{2}m_\rho^2\rho^2 + \frac{1}{2}m_\delta^2\delta^2 + \frac{1}{2}m_\phi^2\phi^2 + \sum_B \varepsilon_{\mathrm{kin}}^B + \sum_l \varepsilon_{\mathrm{kin}}^l,$$
$$P = -\frac{1}{2}m_\sigma^2\sigma^2 + \frac{1}{2}m_\omega^2\omega^2 + \frac{1}{2}m_\rho^2\rho^2 - \frac{1}{2}m_\delta^2\delta^2 + \frac{1}{2}m_\phi^2\phi^2 + \rho\Sigma_N^r + \sum_B P_{\mathrm{kin}}^B + \sum_l P_{\mathrm{kin}}^l, \tag{12}$$

where $\varepsilon_{\mathrm{kin}}^B$ ($\varepsilon_{\mathrm{kin}}^l$) and P_{kin}^B (P_{kin}^l) are the contributions from kinetic energy,

$$\varepsilon_{\mathrm{kin}} = \frac{k_F^4}{\pi^2}\left[\left(1 + \frac{z^2}{2}\right)\frac{\sqrt{1+z^2}}{4} - \frac{z^4}{8}\ln\left(\frac{1+\sqrt{1+z^2}}{z}\right)\right],$$
$$P_{\mathrm{kin}} = \frac{k_F^4}{3\pi^2}\left[\left(1 - \frac{3z^2}{2}\right)\frac{\sqrt{1+z^2}}{4} + \frac{3z^4}{8}\ln\left(\frac{1+\sqrt{1+z^2}}{z}\right)\right], \ z = \frac{1}{q}. \tag{13}$$

Usually, the EoS is the pressure as a function of the energy density. The squared sound velocity v_s^2 is related to EoS by

$$v_s^2 = \frac{\partial P}{\partial\varepsilon}. \tag{14}$$

The mass–radius relation of a stationary neutron star is obtained by solving the Tolman–Oppenheimer–Volkoff (TOV) equation (Oppenheimer & Volkoff 1939; Tolman 1939),

$$\frac{dP}{dr} = -\frac{[P(r) + \varepsilon(r)][M(r) + 4\pi r^3 P(r)]}{r[r - 2M(r)]},$$
$$\frac{dM}{dr} = 4\pi r^2\varepsilon(r), \tag{15}$$

Table 1
Saturation Properties of Nuclear Matter for Different DDRMF Effective Interactions

Effective Interaction (1)	ρ_0 (fm^{-3}) (2)	E/A (MeV) (3)	K_0 (MeV) (4)	E_{sym} (MeV) (5)	L (MeV) (6)	M_n^*/M_n (7)
DD-ME2	0.152	−16.14	251.1	32.30	51.26	0.572
DD-MEδ	0.152	−16.12	219.1	32.35	52.85	0.609
PKDD	0.150	−16.27	262.2	36.86	90.21	0.570
TW99	0.153	−16.25	240.2	32.77	55.31	0.555
DD-MEX	0.152	−16.14	267.1	32.27	49.69	0.556
DDV	0.1511	−16.097	239.5	33.59	69.65	0.586
DDVT	0.1536	−16.924	240.0	31.56	42.35	0.667
DDVTD	0.1536	−16.915	239.9	31.82	42.58	0.667

Note. The saturation properties we list here include the saturation density ρ_0 (fm^{-3}), binding energy per particle E/A (MeV), incompressibility K_0 (MeV), symmetry energy E_{sym} (MeV), slope of symmetry energy L (MeV), and effective mass of the neutron M_n^*/M_n.

Table 2
Coupling Constants between Hyperons and σ for Different DDRMF Effective Interactions

Effective Interaction (1)	$R_{\sigma\Lambda}$ (2)	$R_{\sigma\Sigma}$ (3)	$R_{\sigma\Xi}$ (4)
DD-ME2	0.620035	0.470799	0.315064
DD-MEδ	0.625095	0.461759	0.323150
PKDD	0.620933	0.472392	0.315603
TW99	0.617016	0.473473	0.311023
DD-MEX	0.617628	0.474792	0.311198
DDV	0.622105	0.467624	0.318478
DDVT	0.631152	0.439371	0.335579
DDVTD	0.631716	0.439687	0.335942

with a given EoS as input, where r is the distance from the center. Given a central density ρ_c at $r = 0$, the TOV equation is integrated from $r = 0$ to R where the pressure is zero. Here R is defined as the radius of the neutron star, and $M(R)$ is the gravitational mass.

3. Results and Discussions

3.1. DDRMF Effective Interactions

In this work, the neutron star properties are calculated by using eight DDRMF effective interactions under different assumptions on the interior composition. The δ meson is taken into account in DD-MEδ and DDVTD. The tensor coupling is included in DDVT and DDVTD, but we do not consider its contribution because the tensor coupling effects vanish in nuclear matter (Typel & Terrero 2020). In Table 1, the saturation properties of symmetric nuclear matter calculated with different effective interactions are listed, including the saturation density ρ_0, binding energy per particle E/A, incompressibility K_0, symmetry energy E_{sym}, slope of symmetry energy L, and effective mass of the neutron M_n^*/M_n.

The incompressibility K_0 and slope of symmetry energy L significantly affect the EoS and macroscopic properties (e.g., mass and radius) of neutron stars (Chen & Piekarewicz 2014; Biswal et al. 2019; Ji et al. 2019; Choi et al. 2021). Several constraints on K_0 and L were obtained from terrestrial experiments and astrophysical observations. We first check whether these effective interactions can be ruled out by these constraints. Among the eight effective interactions, the values of K_0 range from 219.1 (DD-MEδ) to 267.1 (DD-MEX) MeV, which satisfies the recent constraint, 215 MeV $\leqslant K_0 \leqslant$ 260 MeV, from Choi et al. (2021) except for PKDD and DD-ME2. For L, the values range from 42.35 (DDVT) to 90.21 (PKDD) MeV, which fulfills the constraints in Oertel et al. (2017; $L = 58.7 \pm 28.1$ MeV) and Choi et al. (2021; 40 MeV $\leqslant L \leqslant$ 85 MeV) except for PKDD. Besides, in Yan (2019), the observations of glitching pulsars were used to constrain the symmetry energy and incompressibility, and it was found that the lower limits of K_0 and L are 215 and 67 MeV, respectively; only PKDD and DDV can meet the constraint of L. Reed et al. obtained a value of $L = 106 \pm 37$ MeV by analyzing the neutron skin thickness of ^{208}Pb (Reed et al. 2021), which is consistent with the lower limit of L in Yan (2019). Due to the uncertainty of these constraints, it is difficult to judge which effective interaction is the best one. Investigating the universal effects of the ϕ meson on hyperon stars by using these effective interactions with large uncertainties of K_0 and L is necessary and meaningful.

3.2. Effects of the ϕ Meson on the Interior Composition

In Table 2, we list the ratio $R_{\sigma Y}$ for different effective interactions. Combined with the hyperon–meson coupling constants given in Table 2 and Equation (10), within a given density range, the baryon and lepton fractions as a function of ρ_B for various effective interactions are obtained by self-consistently solving the NL coupled equations consisting of Equations (3) and (5), the charge neutrality condition, and the baryon number conservation condition. The hyperon thresholds can be easily extracted from the baryon fractions. The hyperon thresholds of the $npe\mu Y$ and $npe\mu Y\phi$ matters calculated with different effective interactions are listed in Table 3 and shown in Figure 1.

For the $npe\mu Y$ matter, within the density range we consider, it is noticed that not all hyperons appear as density increases, and the orders and thresholds of the appearance of various hyperons with different effective interactions are very different. In our calculations, only Λ, Σ^-, Ξ^0, and Ξ^- are likely to be populated. In general, both effective interaction and hyperon properties influence the hyperon thresholds in different manners. This can be understood by the threshold equation

$$\mu_n - q_B\mu_e \geqslant M_B + \Gamma_{\sigma B}\sigma + \Gamma_{\delta B}\delta\tau_3^B + \Gamma_{\omega B}\omega + \Gamma_{\rho B}\rho\tau_3^B. \quad (16)$$

Once the condition in Equation (16) is fulfilled, the hyperon is populated. A hyperon with smaller mass is more mass-favored, according to the first term on the right-hand side. Negatively charged hyperons are charge-favored because they can replace the role of the neutral baryons and leptons at the top of the Fermi sea (Glendenning 1985). A hyperon having the opposite (same) sign as τ_3 of the neutron is isospin-favored when the sign of $\Gamma_{\delta B}\delta + \Gamma_{\rho B}\rho$ is fixed as negative (positive). The hypernuclear potential affects the thresholds by changing $R_{\sigma Y}$ through the relation in Equation (11). The effective interaction mainly determines the behaviors of nucleonic matter before the first hyperon is populated and further affects the hyperon thresholds together with hyperon properties.

Table 3
Hyperon Thresholds Calculated with Different DDRMF Effective Interactions for $npe\mu Y$ and $npe\mu Y\phi$ Matter

Matter	Effective Interaction	First Y		Second Y		Third Y		Fourth Y	
		Y	$\rho_{\rm Thold}$ ($\rm fm^{-3}$)	Y	$\rho_{\rm Thold}$ ($\rm fm^{-3}$)	Y	$\rho_{\rm Thold}$ ($\rm fm^{-3}$)	Y	$\rho_{\rm Thold}$ ($\rm fm^{-3}$)
(1)	(2)	(3)	(4)	(5)	(6)	(7)	(8)	(9)	(10)
$npe\mu Y$	DD-ME2	Λ	0.3314	Ξ^-	0.3684	Σ^-	0.3756	Ξ^0	0.7847
	DD-MEδ	Σ^-	0.3749	Λ	0.3782	Ξ^-	0.4862	Ξ^0	1.3355
	PKDD	Λ	0.3159	Ξ^-	0.3799	Ξ^0	0.8272		
	TW99	Λ	0.3631	Σ^-	0.3907	Ξ^-	0.4369	Ξ^0	1.0359
	DD-MEX	Λ	0.3212	Σ^-	0.3540	Ξ^-	0.3552	Ξ^0	0.7492
	DDV	Λ	0.3386	Ξ^-	0.3985	Σ^-	0.4286	Ξ^0	1.0737
	DDVT	Λ	0.4020	Ξ^-	0.4539	Ξ^0	1.1343		
	DDVTD	Λ	0.3998	Ξ^-	0.4540	Ξ^0	1.1792		
$npe\mu Y\phi$	DD-ME2	Λ	0.3314	Σ^-	0.3745	Ξ^-	0.3764	Ξ^0	1.1580
	DD-MEδ	Σ^-	0.3749	Λ	0.3785	Ξ^-	0.5448		
	PKDD	Λ	0.3159	Ξ^-	0.3957	Σ^-	0.4977	Ξ^0	1.2315
	TW99	Λ	0.3631	Σ^-	0.3925	Ξ^-	0.4733	Ξ^0	1.4821
	DD-MEX	Λ	0.3212	Σ^-	0.3569	Ξ^-	0.3653	Ξ^0	1.1108
	DDV	Λ	0.3386	Ξ^-	0.4119	Σ^-	0.4170	Ξ^0	1.5840
	DDVT	Λ	0.4020	Ξ^-	0.4623	Σ^-	0.5186	Ξ^0	1.6452
	DDVTD	Λ	0.3998	Ξ^-	0.4629	Σ^-	0.5189	Ξ^0	1.7230

Note. Here $\rho_{\rm Thold}$ is the hyperon threshold density.

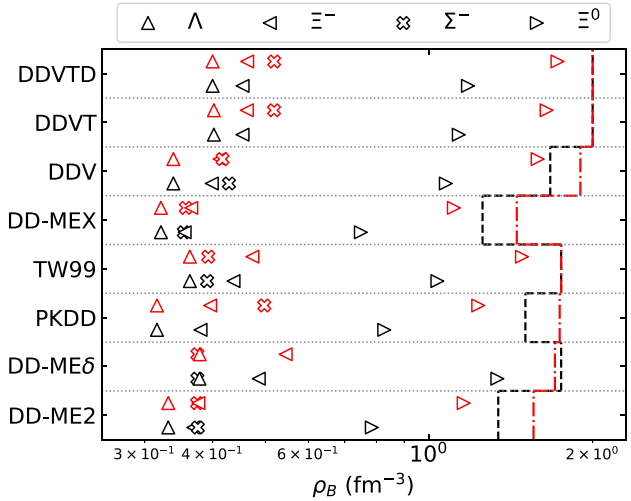

Figure 1. Hyperon thresholds of the $npe\mu Y$ (black symbols) and $npe\mu Y\phi$ (red symbols) matters calculated with different effective interactions. The dashed lines stand for truncation densities before which the maximum masses have been reached.

Now we discuss the effects of the ϕ meson on hyperon thresholds in the $npe\mu Y\phi$ matter. In Figure 2, we show the particle fractions ($X_i = \rho_v^i/\rho_B$, $i = n, p, \Lambda, \Sigma^{\pm,0}$ and $\Xi^{0,-}$) with DD-ME2, PKDD, DDVT, and DDVTD. The main differences in the hyperon thresholds between the $npe\mu Y$ and $npe\mu Y\phi$ matters can be found in Figures 1 and 2 and Table 3: (a) compared with the $npe\mu Y$ matter, the hyperon thresholds of the $npe\mu Y\phi$ matter are shifted to higher densities (especially for Ξ), except for the first appearing hyperon; (b) the order of the thresholds of Σ^- and Ξ^- is reversed after the ϕ meson is included in calculations with DD-ME2; and (c) Σ^- appears in the $npe\mu Y\phi$ matter but not in the $npe\mu Y$ matter with PKDD, DDVT, and DDVTD.

In order to understand the effects of the ϕ meson, we display the total hyperon fraction ($X_Y = \sum_i \rho_v^i/\rho_B$, $i = \Lambda, \Sigma^{\pm,0}$ and $\Xi^{0,-}$) as a function of baryon number density in Figure 3. Taking DD-ME2 as an example, X_Y is reduced significantly when the ϕ meson is considered in comparison with the case of the $npe\mu Y$ matter. The ϕ meson enhances the repulsive interaction between hyperons and increases the energy of hypernuclear matter, causing the reduction of the particle fractions of hyperons that are energy-favored; note that this is also found in the NLRMF model (Banik et al. 2014). The β-equilibrium conditions of the hyperons in Equation (5) can also be used to explain the reduction of X_Y in the $npe\mu Y\phi$ matter. Compared to the $npe\mu Y$ matter, a positive term is added on the right-hand side of the β-equilibrium condition when the ϕ meson is included. To ensure that the β-equilibrium condition is fulfilled, the Fermi momentum of the hyperon needs to become smaller, which leads to the fact that X_Y is reduced. The results and discussions of other effective interactions are similar to those of DD-ME2.

In Figures 1 and 2, we can see that the hyperon thresholds are shifted to higher densities for all effective interactions when the ϕ meson is considered, except for the first appearing hyperon. The ϕ meson mediates the repulsive interaction between hyperons and takes effect only after the first appearing hyperon is populated. Therefore, the first hyperon threshold remains strictly unchanged. For the $npe\mu Y\phi$ matter, the threshold equation of the hyperon species B is written as

$$\mu_n - q_B\mu_e \geqslant M_B + \Gamma_{\sigma B}\sigma + \Gamma_{\delta B}\delta\tau_3^B + \Gamma_{\omega B}\omega + \Gamma_{\rho B}\rho\tau_3^B + \Gamma_{\phi B}\phi. \quad (17)$$

The ϕ meson contributes a positive term to the right-hand side of Equation (16). A larger μ_n at higher density is required due

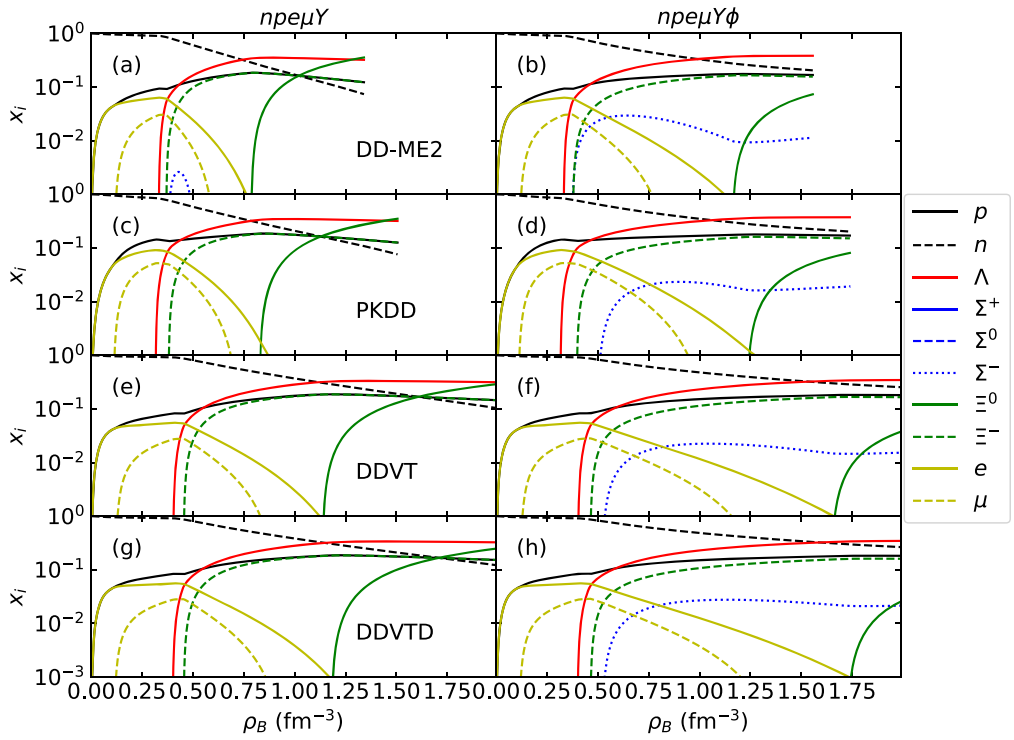

Figure 2. Particle fractions of baryons as a function of baryon number density with DD-ME2, PKDD, DDVT, and DDVTD. Panels (a), (c), (e), and (g) are for the $npe\mu Y$ matter, and panels (b), (d), (f), and (h) are for the $npe\mu Y\phi$ matter. The two panels in the same row represent the results with the same effective interaction. The particle fractions of leptons, defined as ρ_l/ρ_B, as a function of the baryon number density are also plotted as yellow solid lines (electrons) and yellow dotted lines (muons).

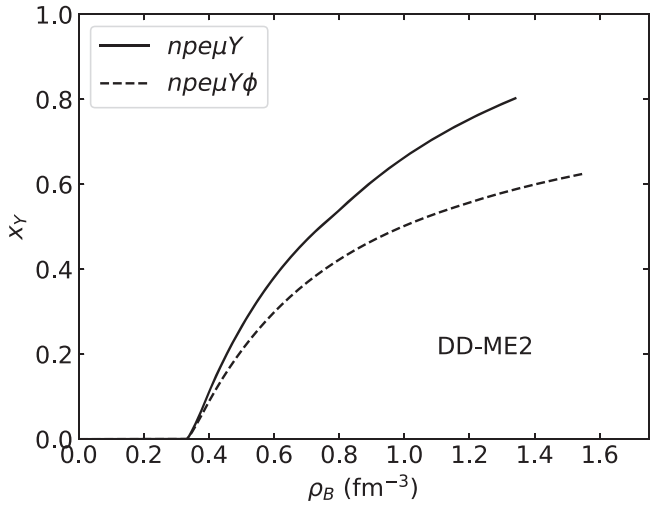

Figure 3. Total hyperon fraction as a function of baryon number density with DD-ME2 in the $npe\mu Y$ and $npe\mu Y\phi$ matters.

to the larger value of the right-hand side in Equation (17), causing the hyperon threshold to be shifted to a higher density.

The ϕ meson has a greater effect on the threshold density of Ξ because its strangeness number is -2, and the coupling strength between Ξ and ϕ is twice that for other hyperons (Providência et al. 2019). This can be used to explain the reversal of the order of hyperon appearance with DD-ME2. The threshold densities of Ξ increase more significantly than those of other hyperons because the contribution of the ϕ meson in Equation (17) for Ξ is twice that of other hyperons. The reason why the order of the appearance of Σ^- and Ξ^- is reversed in the calculations of DD-ME2 is that the ϕ meson has a greater impact on Ξ^-, so that the threshold density of Ξ^- becomes larger than that of Σ^-.

The ϕ meson may change the hyperon species inside neutron stars. To explore the reason why Σ^- appears in the $npe\mu Y\phi$ matter but not in the $npe\mu Y$ matter with PKDD, DDVT, and DDVTD, we show the chemical potentials of baryons as a function of the baryon number density in Figure 4, taking PKDD as an example. In Figure 4, the intersection of the chemical potential of a hyperon and $\mu_n+\mu_e$ or $\mu_n-\mu_e$ means that the corresponding hyperon threshold is reached, and the two chemical potential curves that keep coincident above the threshold density ensure that the β-equilibrium condition is satisfied accordingly. For Σ^- and Ξ^-, their β-equilibrium conditions are $\mu_{\Sigma^-}=\mu_{\Xi^-}=\mu_n+\mu_e$. As we can see in Figures 3 and 4, the total hyperon fraction X_Y is higher for the $npe\mu Y$ matter, and the fraction of the neutron is suppressed so that the Fermi momentum of the neutron and $\mu_n+\mu_e$ rise slowly. For the results calculated with PKDD, μ_{Σ^-} and $\mu_n+\mu_e$ are approximately parallel after Ξ^- is populated. They will not intersect as density increases and do not satisfy the threshold equation. However, X_Y is suppressed when the ϕ meson is considered. The Fermi momentum of the neutron is higher, and $\mu_n+\mu_e$ rises faster than the case without the ϕ meson. The result is that $\mu_n+\mu_e$ can more easily intersect with μ_{Σ^-}, causing Σ^- to appear in the $npe\mu Y\phi$ matter. The changed hyperon species inside neutron stars may affect the cooling properties induced by the hyperons. Similar discussions also hold in the calculation results with DDVT and DDVTD.

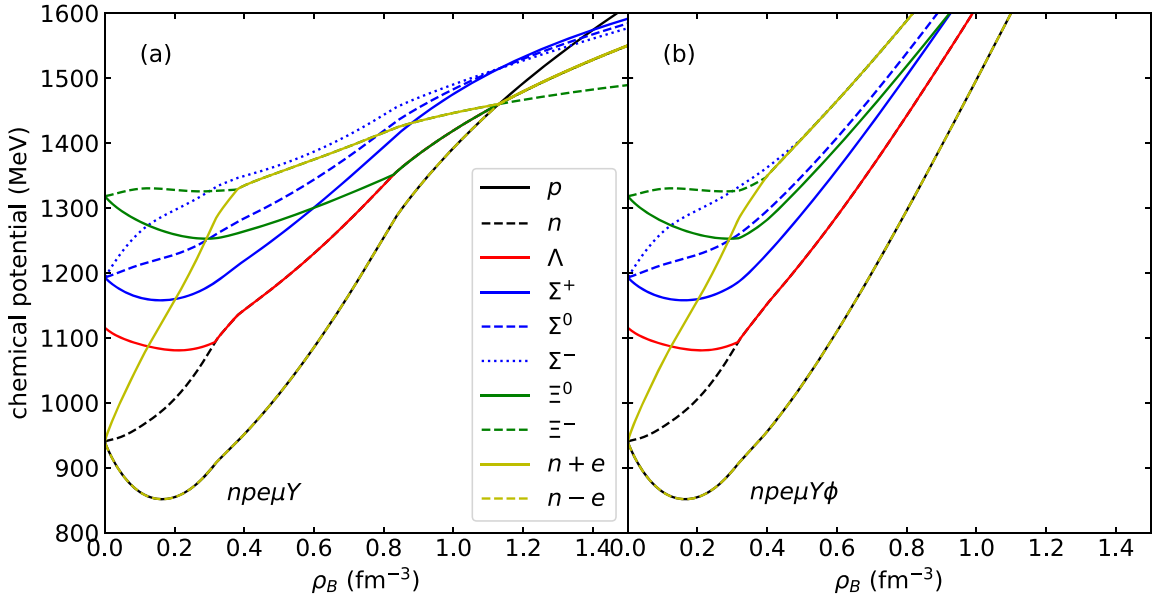

Figure 4. Chemical potential of baryons as a function of baryon number density with PKDD in the $npe\mu Y$ and $npe\mu Y\phi$ matters. The labels "$n + e$" and "$n - e$" represent the two cases of the left-hand side in the first equation of Equation (5), $\mu_n + \mu_e$ and $\mu_n - \mu_e$.

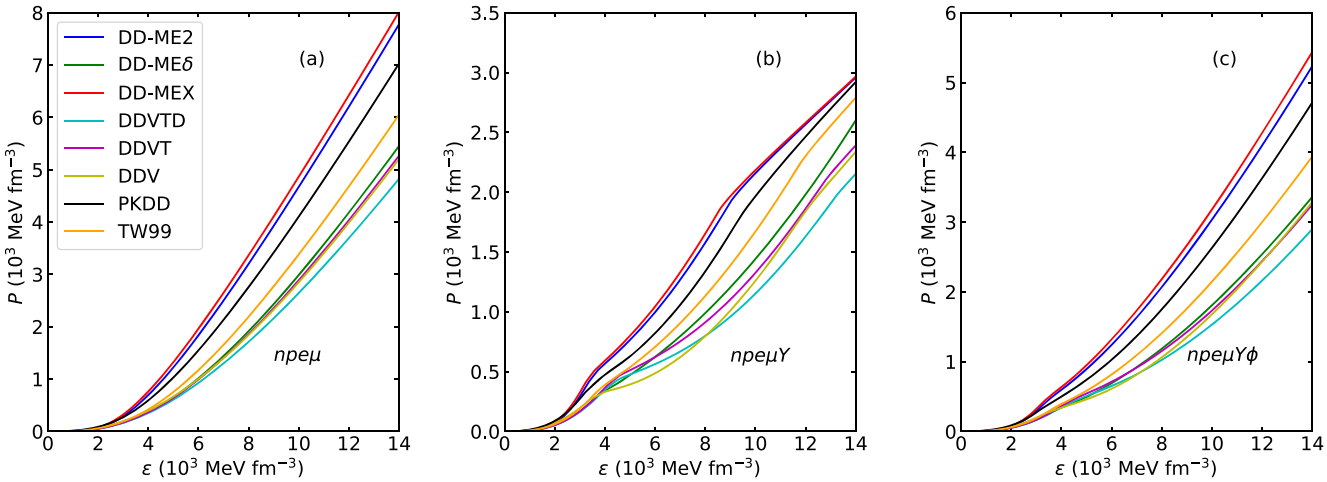

Figure 5. The EoSs of the $npe\mu$, $npe\mu Y$, and $npe\mu Y\phi$ matters with various effective interactions.

3.3. Effects of the ϕ Meson on the EoS and Sound Velocity

The ϕ meson significantly changes the neutron star interior composition and affects the EoS and the sound velocity v_s. In Figure 5, the EoSs of the $npe\mu$, $npe\mu Y$, and $npe\mu Y\phi$ matters calculated with various effective interactions are displayed. For the $npe\mu$ matter, the two stiffest EoSs are given by DD-ME2 and DD-MEX, and the softest EoS is given by DDVTD. Although the saturation properties of the nuclear matter of DDV and DDVT are very different, the EoSs given by them are very close to each other, even at a high energy density. Comparing the EoSs generated with DDVT and DDVTD, the δ meson softens the EoS of asymmetric nuclear matter in the DDRMF model, which is consistent with previous studies (Liu et al. 2007, 2008; Wang et al. 2014).

The appearance of hyperons in the $npe\mu Y$ matter leads to a strong softening of the EoSs for all effective interactions. The DD-ME2 and DD-MEX still give the two stiffest EoSs. The pressure calculated with DD-MEX is obviously larger than that calculated with DD-ME2 at a low energy density, but there is little difference at a high energy density. The softest EoS is given by DDV at a low energy density, but DDVTD generates the softest EoS at a high energy density. The EoS calculated with DDVT is significantly stiffer than that calculated with DDV at a low energy density compared to the $npe\mu$ matter. For all effective interactions, the EoSs of the $npe\mu Y\phi$ matter are stiffer than those of the $npe\mu Y$ matter, but they are still softer than those of the $npe\mu$ matter. The ϕ meson shifts the hyperon thresholds to higher densities and suppresses the hyperon fractions, causing a weaker softening of the total EoS.

The squared sound velocity v_s^2 can be easily obtained from the EoS by using Equation (14). The causal limit $v_s^2 < 1$ (Dutra et al. 2016) and the conformal limit $v_s^2 < 1/3$ (Bedaque & Steiner 2015) are used to constrain the sound velocity. In Figure 6, we show the squared sound velocities as a function of ρ/ρ_0 for the $npe\mu$, $npe\mu Y$, and $npe\mu Y\phi$ matters with various effective interactions. For the $npe\mu$ matter, the sound velocities calculated with all effective interactions satisfy the causal limit, but they exceed the conformal limit. A stiffer EoS leads to a higher sound velocity. For the $npe\mu Y$ matter, the sound velocity

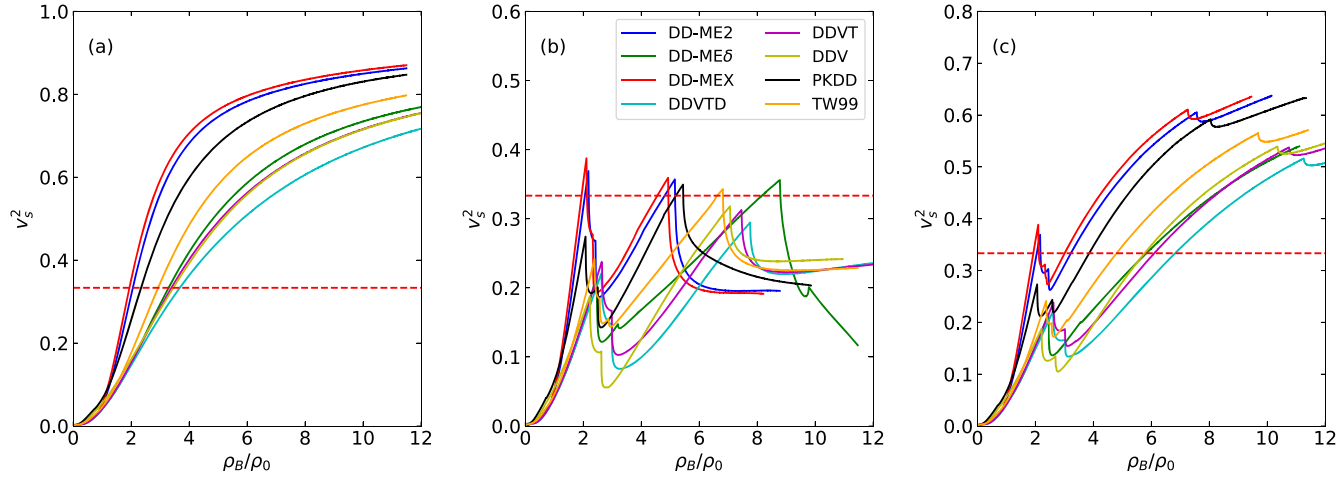

Figure 6. Squared sound velocity as a function of ρ_B/ρ_0 for the $npe\mu$, $npe\mu Y$, and $npe\mu Y\phi$ matters with various effective interactions. The dashed line represents the conformal limit $v_s^2 = 1/3$.

is reduced because hyperons soften the corresponding EoS. The causal limit is also fulfilled for all effective interactions, but the squared sound velocities exceed the conformal limit around some hyperon thresholds and are less than one-third at high density. We also notice that the sound velocity shows a peak at the threshold density of every individual hyperon because the onset of hyperons suddenly softens the EoS (Lopes & Menezes 2014). Unlike the $npe\mu$ matter, it seems impossible to draw the conclusion that the stiffer EoS leads to a larger sound velocity; e.g., the sound velocity calculated with PKDD is smaller than that of DDVTD, but the EoS calculated with PKDD is significantly stiffer than that calculated with DDVTD. For the $npe\mu Y\phi$ matter, the sound velocities calculated with all effective interactions satisfy the causal limit, but the conformal limit is exceeded at high density. The ϕ meson suppresses the hyperon fractions of the $npe\mu Y\phi$ matter and weakens the rapid reduction of sound velocity caused by the softening of a related EoS. Meanwhile, the increased hyperon thresholds make the sound velocity increase again in a larger density range, which leads to the conformal limit being exceeded.

3.4. Effects of the ϕ Meson on the Mass–Radius Relation

The ϕ meson has an impact on the macroscopic properties of neutron stars that are closely related to the EoS. The mass–radius relation of a static neutron star is obtained by solving the TOV Equation (15) with a given EoS as input. The BPS (Baym et al. 1971) and BBP (Baym et al. 1971) EoSs are chosen as the EoSs of the outer and inner crusts of neutron stars, respectively. Taking DD-ME2 as an example, the mass–radius relations of neutron stars are shown in Figure 7. The largest maximum mass of neutron stars is obtained by using the EoS without hyperons. The smallest maximum mass of neutron stars is obtained by using the EoS with hyperons but without the ϕ meson. The maximum mass of $npe\mu Y\phi$ neutron stars is larger than that of $npe\mu Y$ neutron stars but smaller than that of $npe\mu$ neutron stars because the stiffness of the EoS with hyperons and the ϕ meson is between that of the EoS with hyperons but without the ϕ meson and that of the EoS without hyperons. Results calculated with other effective interactions show similar characteristics to those calculated with DD-ME2.

In Figure 8, the mass–radius relations of neutron stars calculated with various effective interactions for $npe\mu$, $npe\mu Y$, and $npe\mu Y\phi$ neutron stars are shown. The corresponding neutron

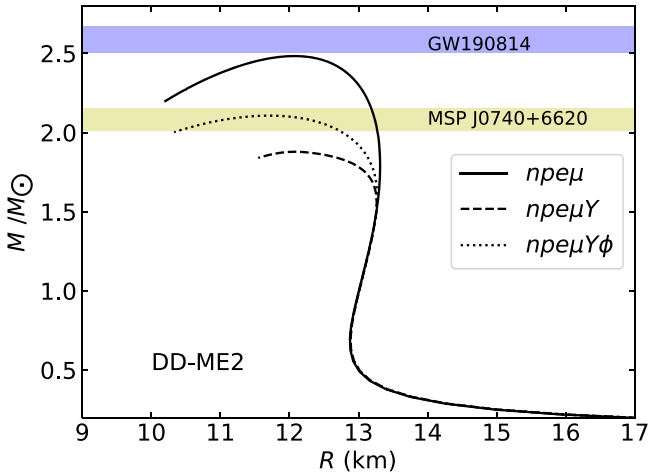

Figure 7. Mass–radius relations of $npe\mu$, $npe\mu Y$, and $npe\mu Y\phi$ neutron stars calculated with DD-ME2.

star properties are listed in Table 4. Based on chiral effective field theory interactions, a radius constraint on the canonical $1.4\,M_\odot$ neutron star with $9.7\ \mathrm{km} \leqslant R_{1.4M_\odot} \leqslant 13.9$ km was given in Hebeler et al. (2010). From Table 4, most of our results are compatible with this prediction. The mass of PSR J0030+0451 from NICER is close to the canonical neutron star mass, as shown in the dark green and dark cyan error bars in Figure 8. It can be found that the mass–radius relations of $npe\mu$ neutron stars calculated with all effective interactions agree well with the observations from NICER. But DD-MEδ, DDV, DDVT, and DDVTD are excluded by the constraints from NICER for both $npe\mu Y$ and $npe\mu Y\phi$ neutron stars. The ϕ meson does not seem to significantly affect the radius constraint.

There exists a strong tension between the existence of neutron stars with mass around $2\,M_\odot$ and the conformal limit (Bedaque & Steiner 2015). The large sound velocity that violates the conformal limit may appear inside neutron star cores with the constraints of astrophysical observations (Tews et al. 2018; Reed & Horowitz 2020). Alsing et al. (2018) found the lower bound on the maximum sound velocity of $v_s^{\max} > 0.63$ inside neutron stars so that the conformal limit is significantly broken. However, Ma & Rho (2019) developed the pseudoconformal model and found that the maximum mass constraint of $2.3\,M_\odot$ is accommodated by

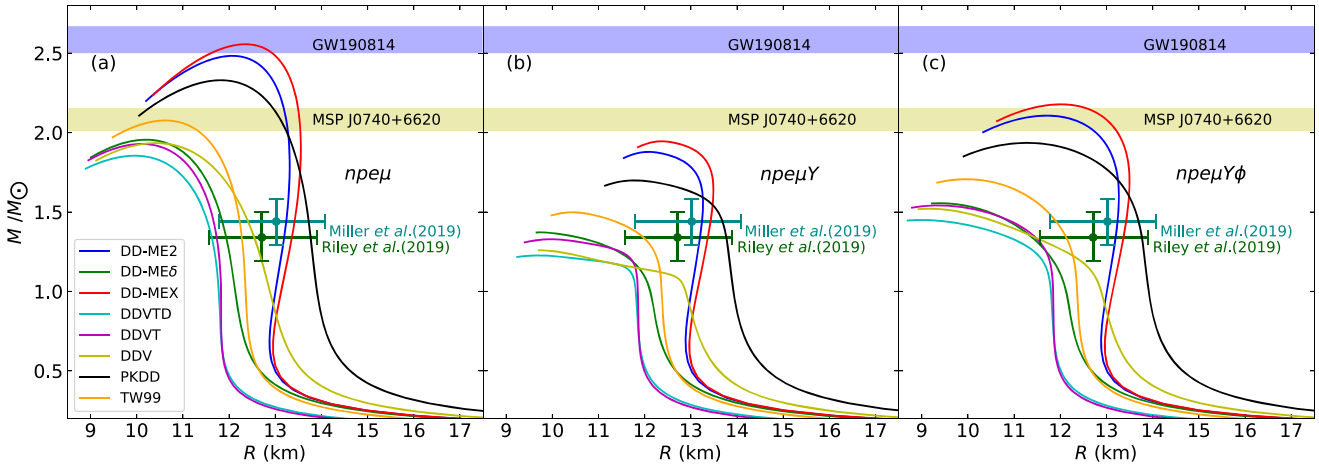

Figure 8. Mass–radius relations of $npe\mu$, $npe\mu Y$, and $npe\mu Y\phi$ neutron stars calculated with various effective interactions. The constraints from the astrophysical observables of MSP J0740+6620 (yellow area), the secondary object of GW190814 (blue area), and the mass and radius of PSR J0030+0451 from NICER in Riley et al. (2019; dark green error bar) and Miller et al. (2019; dark cyan error bar) are shown.

Table 4
Properties of $npe\mu$, $npe\mu Y$, and $npe\mu Y\phi$ Neutron Stars Calculated with Various Effective Interactions

Effective Interaction	$M_{\max}$ ($M_\odot$)	R (km)	ρ_c (fm^{-3})	$R_{1.4M_\odot}$ (km)	$M_{\max}$ ($M_\odot$)	R (km)	ρ_c (fm^{-3})	$R_{1.4M_\odot}$ (km)	$M_{\max}$ ($M_\odot$)	R (km)	ρ_c (fm^{-3})	$R_{1.4M_\odot}$ (km)
	$npe\mu$				$npe\mu Y$				$npe\mu Y\phi$			
(1)	(2)	(3)	(4)	(5)	(6)	(7)	(8)	(9)	(10)	(11)	(12)	(13)
DD-ME2	2.483	12.060	0.82	13.237	1.879	12.081	0.90	13.240	2.107	11.719	0.93	13.239
DD-MEδ	1.955	10.207	1.21	11.852	1.373	9.769	1.55	⋯	1.555	9.386	1.59	10.896
PKDD	2.330	11.808	0.89	13.725	1.699	11.781	1.02	13.684	1.935	11.297	1.06	13.695
TW99	2.076	10.615	1.10	12.228	1.498	10.447	1.29	11.369	1.706	9.980	1.36	11.911
DD-MEX	2.556	12.374	0.77	13.419	1.945	12.364	0.85	13.424	2.178	12.010	0.88	13.424
DDV	1.934	10.405	1.20	12.409	>1.259	<9.706	>1.65	⋯	1.521	9.177	1.71	10.588
DDVT	1.929	10.111	1.23	11.664	1.329	9.975	1.44	⋯	1.541	9.361	1.59	10.944
DDVTD	1.855	9.953	1.29	11.529	1.227	9.714	1.56	⋯	1.450	8.992	1.77	9.537

Note. Here $M_{\max}$, R, ρ_c, and $R_{1.4M_\odot}$ denote maximum mass, radius corresponding to maximum mass, central density, and radius of the neutron star at 1.4 $M_\odot$, respectively.

setting in the conformal limit at $\rho_B \gtrsim 2\rho_0$. In the present work, although the ϕ meson decreases the sound velocity inside neutron stars, the tension mentioned above has not been resolved in the DDRMF model. In Table 4 and Figure 6, we can see that the conformal limit is broken in neutron stars whose maximum masses reach 2 $M_\odot$.

The MSP J0740+6620 with $2.08^{+0.07}_{-0.07} M_\odot$ (68.3% credibility interval; Fonseca et al. 2021) is used to constrain the maximum mass of neutron stars in the present work. From Figure 8 and Table 4, MSP J0740+6620 can rule out DD-MEδ, DDV, DDVT, and DDVTD for $npe\mu$ neutron stars; for $npe\mu Y$ neutron stars, all effective interactions are ruled out because none of them give a maximum mass larger than the lower bound of mass of MSP J0740+6620; and for $npe\mu Y\phi$ neutron stars, the maximum masses calculated with DD-ME2 and DD-MEX are compatible with the observed mass range of MSP J0740+6620, while other effective interactions are excluded. Although the ϕ meson increases the maximum mass of the neutron stars, only a few effective interactions survive under the constraints of astrophysical observations.

The GW190814 event, which is a compact binary merger involving a 22.2–24.3 $M_\odot$ black hole (BH) and a compact object of 2.50–2.67 $M_\odot$, was detected by LIGO/Virgo in 2019 August (Abbott et al. 2020). Whether the secondary object of GW190814 is a massive neutron star or a low-mass BH remains controversial. Huang et al. (2020) suggested that the possibility of the secondary object of GW190814 being a neutron star consisting of hadron matter is not excluded in the DDRMF model. Zhang & Li (2020) found that the secondary object of GW190814 could be a massive pulsar with the highest rotational frequency ever observed, and several following studies indicated that this pulsar may have a quark or hyperonic core (Dexheimer et al. 2021; Rather et al. 2021b). The R-mode stability of this superfast pulsar is supported by Zhou et al. (2021). The possibility of the secondary object of GW190814 being a hyperon star or low-mass BH was studied in Sedrakian et al. (2020) and Li et al. (2020), and it was implied that the GW190814 event was likely to be a binary BH merger rather than a neutron star–BH merger. Recently, the possibilities of a strange quark star (Bombaci et al. 2021), an up–down quark star (Cao et al. 2020), and a dark matter admixed neutron star (Das et al. 2021) were also proposed. In the present work, DD-ME2 and DD-MEX support the idea that the secondary object of GW190814 is a neutron star without hyperons, similar to the conclusion drawn in Huang et al. (2020). However, there are no effective interactions supporting it as a hyperon star whether or not the ϕ meson is considered.

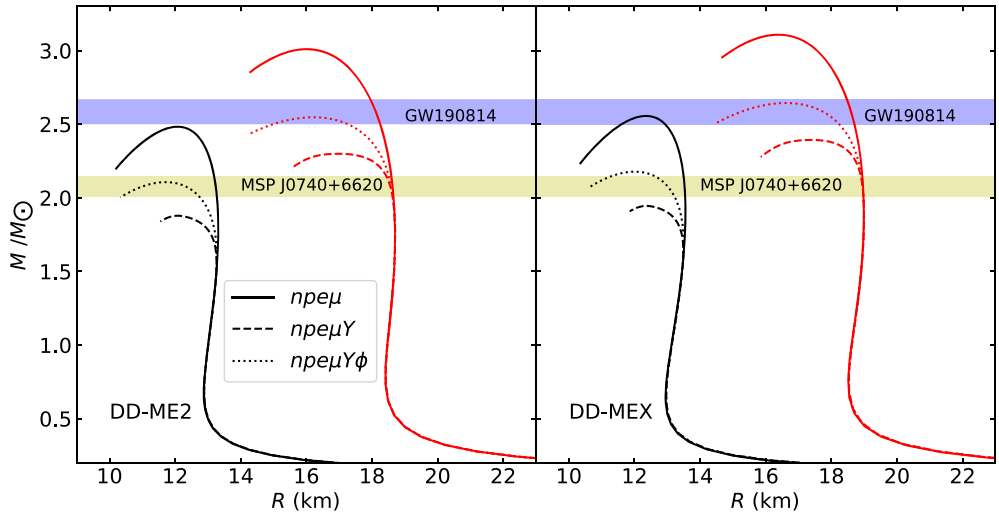

Figure 9. Mass–radius relations of nonrotating (black lines) and Keplerian rotating (red lines) neutron stars calculated with DD-ME2 and DD-MEX for $npe\mu$, $npe\mu Y$, and $npe\mu Y\phi$ neutron stars.

Table 5
Properties of Static and Keplerian Rotating $npe\mu$, $npe\mu Y$, and $npe\mu Y\phi$ Neutron Stars Calculated with DD-ME2 and DD-MEX

	Static Neutron Stars						Keplerian Rotating Neutron Stars					
	DD-ME2			DD-MEX			DD-ME2			DD-MEX		
(1)	$npe\mu$ (2)	$npe\mu Y$ (3)	$npe\mu Y\phi$ (4)	$npe\mu$ (5)	$npe\mu Y$ (6)	$npe\mu Y\phi$ (7)	$npe\mu$ (8)	$npe\mu Y$ (9)	$npe\mu Y\phi$ (10)	$npe\mu$ (11)	$npe\mu Y$ (12)	$npe\mu Y\phi$ (13)
$M_{\max}$ ($M_\odot$)	2.483	1.879	2.107	2.556	1.945	2.178	3.010	2.300	2.548	3.108	2.394	2.645
R (km)	12.060	12.081	11.719	12.374	12.364	12.010	16.005	16.989	16.215	16.377	17.402	16.618
ρ_c (fm^{-3})	0.82	0.90	0.93	0.77	0.85	0.88	0.73	0.73	0.79	0.69	0.69	0.74
$R_{1.4M_\odot}$ (km)	13.237	13.240	13.239	13.419	13.424	13.424	18.640	18.640	18.640	18.859	18.862	18.861
$z_{\rm surf}$	0.206	0.206	0.206	0.202	0.202	0.202	…	…	…	…	…	—
z_p	…	…	…	…	…	…	0.221	0.221	0.221	0.218	0.217	0.217
z_f	…	…	…	…	…	…	−0.238	−0.238	−0.238	−0.237	−0.237	−0.237
z_b	…	…	…	…	…	…	0.700	0.700	0.700	0.692	0.691	0.691

Note. The definitions of $M_{\max}$ and ρ_c are the same as those in Table 4. Here R and $R_{1.4M_\odot}$ are the equatorial radii of the neutron star with maximum mass and the canonical neutron star, respectively; $z_{\rm surf}$ is the surface gravitational redshift of the static neutron star; and z_p, z_f, and z_b are the polar redshift, equatorial redshift in the forward direction, and equatorial redshift in the backward direction of the rapidly rotating neutron star, respectively.

As is well known, the rotation of neutron stars can increase the maximum mass by about 20% (Weber & Glendenning 1992; Cook et al. 1994; Paschalidis & Stergioulas 2017). For the static counterpart of the secondary object in GW190814, the lower limit on its maximum mass is around 2.08 $M_\odot$ (Most et al. 2020). From Table 4, we note that the maximum masses of $npe\mu Y\phi$ neutron stars calculated with DD-ME2 and DD-MEX exceed 2.1 $M_\odot$; hence, the two effective interactions support the possibility of the secondary object of GW190814 being a rotating $npe\mu Y\phi$ neutron star. In order to verify this possibility, using the previous EoSs calculated with DD-ME2 and DD-MEX, it is necessary to calculate the global properties of neutron stars rotating with the Kepler frequency. For a uniformly rotating neutron star with an axisymmetric configuration, the metric tensor, which describes its geometry, is given by

$$ds^2 = -e^{2\nu(r,\theta)}dt^2 + e^{2\psi(r,\theta)}[d\phi - \omega(r)dt] + e^{2\mu(r,\theta)}d\theta^2 + e^{2\lambda(r,\theta)}dr^2, \quad (18)$$

where the gravitational potentials ν, ψ, μ, and λ depend on the radial variable r and azimuthal angle θ but independent of time t and polar angle ϕ (Butterworth & Ipser 1976; Friedman et al. 1986). The RNS code (Cook et al. 1994; Stergioulas & Friedman 1995), which is based on the Komatsu–Eriguchi–Hachisu method (Komatsu et al. 1989), iteratively solves the Einstein field equations and hydrostatic equilibrium equation and gives the numerical solution of the equilibrium structure of a rotating neutron star. The rotation is taken into account by deforming a neutron star from a spherical configuration to an axisymmetric configuration. The Kepler frequency of a stable neutron star is the maximum spin frequency above which the mass escapes from its surface (Rather et al. 2021b). The surface gravitational redshift, which is related to the compactness M/R, can be used to constrain the EoSs of neutron stars. The surface gravitational redshift $z_{\rm surf}$ of the canonical static neutron star is calculated as $z_{\rm surf} = (1 - 2M/R)^{-1/2} - 1$ (Tolos et al. 2017). For a rapidly rotating neutron star, the polar redshift z_p, equatorial redshift in the backward direction z_b, and equatorial

redshift in the forward direction z_f are obtained by using the equations taken from Appendix B in Cook et al. (1994).

In Figure 9, we display the mass–radius relations of static and Keplerian rotating neutron stars with DD-ME2 and DD-MEX. The maximum masses of neutron stars at Kepler frequencies are larger than their static counterparts. A rotating neutron star has a larger equatorial radius than its static counterpart for both the canonical and neutron stars with maximum mass. The properties of static and Keplerian rotating neutron stars calculated with DD-ME2 and DD-MEX are given for comparison in Table 5. The rotations of neutron stars increase their maximum masses by 20.9%–23.1%. The gravitational redshifts of $npe\mu$, $npe\mu Y$, and $npe\mu Y\phi$ neutron stars are almost the same for DD-ME2 and DD-MEX because the effects of hyperons and the ϕ meson are weak inside the canonical neutron star cores. Hebeler et al. (2010) gave a gravitational redshift range of $z = 0.193$–0.320 and an observational limit of $z = 0.12$–0.23 from 1E 1207.4–5209, presented in Sanwal et al. (2002). From our results, both the $z_{\rm surf}$ of static neutron stars and the polar redshift z_p of Keplerian rotating neutron stars match the values from space telescopes (Douchin & Haensel 2001; Sanwal et al. 2002). From the maximum masses listed in Table 5, DD-ME2 and DD-MEX support the possibility that GW190814's secondary object is a hyperon star spinning faster than 1264 and 1170 Hz, respectively, but an important prerequisite is that the ϕ meson should be included.

4. Summary

The effects of the ϕ meson on the properties of hyperon stars have been studied systematically in the DDRMF model. The widely used (DD-ME2, DD-MEδ, PKDD, and TW99) and the latest proposed (DD-MEX, DDV, DDVT, and DDVTD) effective interactions were applied to calculate the interior compositions, EoSs, sound velocities, and mass–radius relations of neutron stars.

Similar to the previous works (Banik et al. 2014; Biswal et al. 2019; Lopes & Menezes 2020), since the ϕ meson mediates the repulsive interaction between hyperons, the hyperon thresholds are shifted to higher densities, and the total hyperon fraction decreases when the ϕ meson is included. The ϕ meson has a greater impact on the Ξ hyperon because its strangeness number is -2, and the coupling strength between Ξ and ϕ is twice that of other hyperons. The reversal of the order of hyperon thresholds and the emergence of Σ^- in the $npe\mu Y\phi$ matter are explained by the effects of the ϕ meson on hypernuclear matter.

Because the hyperon composition is suppressed in the $npe\mu Y\phi$ matter, the ϕ meson significantly stiffens the EoSs and causes the sound velocity to exceed the conformal limit. The tension between the conformal limit and the existence of neutron stars with $2\,M_\odot$ still exists in this work, because the conformal limit is broken in neutron stars whose maximum masses reach $2\,M_\odot$.

The ϕ meson increases the maximum mass of neutron stars due to the stiffening of the corresponding EoSs in the DDRMF model, which is consistent with earlier conclusions (Weissenborn et al. 2012b; Banik et al. 2014; Biswal et al. 2019; Lopes & Menezes 2020). For neutron stars with a hyperon but without the ϕ meson, the mass of PSR J0740+6620 rules out all effective interactions used in the present work. However, DD-ME2 and DD-MEX survive under the mass constraint from PSR J0740 +6620 when the ϕ meson is included. For the secondary object of GW190814, whether or not we consider the ϕ meson, our results do not support it as a hyperon star, but two effective interactions, i.e., DD-ME2 and DD-MEX, support the possibility that it is an $npe\mu Y\phi$ neutron star rotating with Kepler frequency.

Helpful discussions with Johann Haidenbauer, Hoai Le, and Andreas Nogga are gratefully acknowledged. We thank Xiang-Xiang Sun and Yu-Ting Rong for reading the manuscript and valuable suggestions. This work has been supported by the National Key R&D Program of China (grant No. 2018YFA0404402), the National Natural Science Foundation of China (grant Nos. 11525524, 12070131001, 12047503, and 11961141004), the Key Research Program of Frontier Sciences of the Chinese Academy of Sciences (grant No. QYZDB-SSWSYS013), the Strategic Priority Research Program of the Chinese Academy of Sciences (grant Nos. XDB34010000 and XDPB15), and the IAEA Coordinated Research Project (grant No. F41033). The results described in this paper were obtained on the High-Performance Computing Cluster of ITP-CAS and the ScGrid of the Supercomputing Center, Computer Network Information Center of the Chinese Academy of Sciences.

ORCID iDs

Zhong-Hao Tu https://orcid.org/0000-0001-6836-9339
Shan-Gui Zhou https://orcid.org/0000-0003-4753-3325

References

Abbott, B., Abbott, R., Abbott, T., et al. 2017, PhRvL, 119, 161101
Abbott, B. P., Abbott, R., Abbott, T. D., et al. 2018, PhRvL, 121, 161101
Abbott, R., Abbott, T. D., Abraham, S., et al. 2020, ApJL, 896, L44
Alford, M. G., Han, S., & Prakash, M. 2013, PhRvD, 88, 083013
Alsing, J., Silva, H. O., & Berti, E. 2018, MNRAS, 478, 1377
Antoniadis, J., Freire, P. C. C., Wex, N., et al. 2013, Sci, 340, 1233232
Baldo, M., & Maieron, C. 2004, PhRvC, 69, 014301
Baldo, M., Polls, A., Rios, A., Schulze, H.-J., & Vidaña, I. 2012, PhRvC, 86, 064001
Banik, S., Hempel, M., & Bandyopadhyay, D. 2014, ApJS, 214, 22
Baym, G., Bethe, H. A., & Pethick, C. J. 1971, NuPhA, 175, 225
Baym, G., Pethick, C., & Sutherland, P. 1971, ApJ, 170, 299
Bedaque, P., & Steiner, A. W. 2015, PhRvL, 114, 031103
Bender, M., Heenen, P.-H., & Reinhard, P.-G. 2003, RvMP, 75, 121
Bhuyan, M., Carlson, B. V., Patra, S. K., & Zhou, S.-G. 2017, IJMPE, 26, 1750052
Biswal, S. K., Patra, S. K., & Zhou, S. G. 2019, ApJ, 885, 25
Bogdanov, S., Guillot, S., Ray, P. S., et al. 2019a, ApJL, 887, L25
Bogdanov, S., Lamb, F. K., Mahmoodifar, S., et al. 2019b, ApJL, 887, L26
Boguta, J., & Bodmer, A. 1977, NuPhA, 292, 413
Bombaci, I., Drago, A., Logoteta, D., Pagliara, G., & Vidaña, I. 2021, PhRvL, 126, 162702
Bombaci, I., Fabrocini, A., Polls, A., & Vidaña, I. 2005, NuPhB, 609, 232
Bonanno, L., & Sedrakian, A. 2012, A&A, 539, A16
Butterworth, E. M., & Ipser, J. R. 1976, ApJ, 204, 200
Cao, Z., Chen, L.-W., Chu, P.-C., & Zhou, Y. 2020, arXiv:2009.00942
Carlson, J., Gandolfi, S., Pederiva, F., et al. 2015, RvMP, 87, 1067
Chen, W.-C., & Piekarewicz, J. 2014, PhRvC, 90, 044305
Chin, S., & Walecka, J. 1974, NuPhB, 52, 24
Choi, S., Miyatsu, T., Cheoun, M.-K., & Saito, K. 2021, ApJ, 909, 156
Cook, G. B., Shapiro, S. L., & Teukolsky, S. A. 1994, ApJ, 424, 823
Das, H., Kumar, A., & Patra, S. 2021, PhRvD, 104, 063028
de Jong, F., & Lenske, H. 1998, PhRvC, 57, 3099
Demorest, P. B., Pennucci, T., Ransom, S. M., Roberts, M. S. E., & Hessels, J. W. T. 2010, Natur, 467, 1081
Dexheimer, V., Gomes, R. O., Klähn, T., Han, S., & Salinas, M. 2021, PhRvC, 103, 025808
Dickhoff, W., & Barbieri, C. 2004, PrPNP, 52, 377
Douchin, F., & Haensel, P. 2001, A&A, 380, 151
Drago, A., Lavagno, A., Pagliara, G., & Pigato, D. 2014, PhRvC, 90, 065809

Dutra, M., Lourenço, O., Avancini, S. S., et al. 2014, PhRvC, 90, 055203
Dutra, M., Lourenço, O., & Menezes, D. P. 2016, PhRvC, 93, 025806
Dutra, M., Lourenço, O., Sá Martins, J. S., et al. 2012, PhRvC, 85, 035201
Fonseca, E., Cromartie, H. T., Pennucci, T. T., et al. 2021, ApJL, 915, L12
Fortin, M., Avancini, S. S., Providência, C., & Vidaña, I. 2017, PhRvC, 95, 065803
Friedman, J. L., Parker, L., & Ipser, J. R. 1986, ApJ, 304, 115
Fuchs, C., Lenske, H., & Wolter, H. H. 1995, PhRvC, 52, 3043
Gendreau, K., & Arzoumanian, Z. 2017, NatAs, 1, 895
Glendenning, N. K. 1985, ApJ, 293, 470
Glendenning, N. K. 1996, Compact Stars: Nuclear Physics, Particle Physics and General Relativity (New York: Springer)
Hebeler, K., Lattimer, J. M., Pethick, C. J., & Schwenk, A. 2010, PhRvL, 105, 161102
Hong, B., Ren, Z.-Z., & Bai, D. 2019, CoTPh, 71, 819
Huang, K., Hu, J., Zhang, Y., & Shen, H. 2020, ApJ, 904, 39
Ishizuka, C., Ohnishi, A., Tsubakihara, K., Sumiyoshi, K., & Yamada, S. 2008, JPhG, 35, 085201
Ji, F., Hu, J., Bao, S., & Shen, H. 2019, PhRvC, 100, 045801
Jiang, J.-L., Tang, S.-P., Wang, Y.-Z., Fan, Y.-Z., & Wei, D.-M. 2020, ApJ, 892, 55
Katayama, T., & Saito, K. 2015, NuPhB, 747, 43
Klähn, T., Łastowiecki, R., & Blaschke, D. 2013, PhRvD, 88, 085001
Komatsu, H., Eriguchi, Y., & Hachisu, I. 1989, MNRAS, 237, 355
Lalazissis, G. A., Nikšić, T., Vretenar, D., & Ring, P. 2005, PhRvC, 71, 024312
Lee, D. 2009, PrPNP, 63, 117
Li, A., Burgio, G. F., Lombardo, U., & Zuo, W. 2006, PhRvC, 74, 055801
Li, A., Dong, J. M., Wang, J. B., & Xu, R. X. 2016, ApJS, 223, 16
Li, A., Zhou, X. R., Burgio, G. F., & Schulze, H. J. 2010, PhRvC, 81, 025806
Li, A., Zuo, W., Mi, A.-J., & Burgio, G. 2007, ChPhB, 16, 1934
Li, J. J., Sedrakian, A., & Weber, F. 2018, NuPhB, 783, 234
Li, J. J., Sedrakian, A., & Weber, F. 2020, NuPhB, 810, 135812
Lim, Y., Kwak, K., Hyun, C. H., & Lee, C.-H. 2014, PhRvC, 89, 055804
Liu, B., Cai-Wan, S., Toro, M. D., & En-Guang, Z. 2008, CoTPh, 49, 199
Liu, B., Toro, M. D., Greco, V., et al. 2007, PhRvC, 75, 048801
Lonardoni, D., Lovato, A., Gandolfi, S., & Pederiva, F. 2015, PhRvL, 114, 092301
Long, W., Meng, J., Giai, N. V., & Zhou, S.-G. 2004, PhRvC, 69, 034319
Lopes, L. L., & Menezes, D. P. 2014, PhRvC, 89, 025805
Lopes, L. L., & Menezes, D. P. 2020, EPJA, 56, 122
Lopes, L. L., & Menezes, D. P. 2021, NuPhA, 1009, 122171
Ma, Y.-L., & Rho, M. 2019, PhRvD, 100, 114003
Maslov, K., Kolomeitsev, E., & Voskresensky, D. 2015, NuPhB, 748, 369
Maslov, K., Yasutake, N., Blaschke, D., et al. 2019, PhRvC, 100, 025802
Meng, J., Ring, P., & Zhao, P. 2016, Relativistic Density Functional for Nuclear Structure (Singapore: World Scientific), 21
Meng, J., Toki, H., Zhou, S., et al. 2006, PrPNP, 57, 470
Meng, J., & Zhou, S. G. 2015, JPhG, 42, 093101
Miller, M. C., Lamb, F. K., Dittmann, A. J., et al. 2019, ApJL, 887, L24
Most, E. R., Papenfort, L. J., Weih, L. R., & Rezzolla, L. 2020, MNRAS: Lett., 499, L82
Mu, X., Jia, H., Zhou, X., & Wang, H. 2017, ApJ, 846, 140
Nikšić, T., Vretenar, D., & Ring, P. 2011, PrPNP, 66, 519
Oertel, M., Hempel, M., Klähn, T., & Typel, S. 2017, RvMP, 89, 015007
Oertel, M., Providência, C., Gulminelli, F., & Raduta, A. R. 2015, JPhG, 42, 075202
Oppenheimer, J. R., & Volkoff, G. M. 1939, PhRv, 055, 374
Paschalidis, V., & Stergioulas, N. 2017, Living Rev. Relativity, 20, 7
Providência, C., Fortin, M., Pais, H., & Rabhi, A. 2019, Front. Astron. Space Sci., 6, 13
Raaijmakers, G., Greif, S. K., Riley, T. E., et al. 2020, ApJL, 893, L21
Rather, I. A., Rahaman, U., Dexheimer, V., Usmani, A. A., & Patra, S. K. 2021a, ApJ, 917, 46
Rather, I. A., Rahaman, U., Imran, M., et al. 2021b, PhRvC, 103, 055814
Reed, B., & Horowitz, C. J. 2020, PhRvC, 101, 045803
Reed, B. T., Fattoyev, F. J., Horowitz, C. J., & Piekarewicz, J. 2021, PhRvL, 126, 172503
Reinhard, P. G. 1989, Rep. Prog. Phys., 52, 439
Rikovska Stone, J., Miller, J. C., Koncewicz, R., Stevenson, P. D., & Strayer, M. R. 2003, PhRvC, 68, 034324
Riley, T. E., Watts, A. L., Bogdanov, S., et al. 2019, ApJL, 887, L21
Ring, P. 1996, PrPNP, 37, 193
Roca-Maza, X., Viñas, X., Centelles, M., Ring, P., & Schuck, P. 2011, PhRvC, 84, 054309
Sanwal, D., Pavlov, G. G., Zavlin, V. E., & Teter, M. A. 2002, ApJ, 574, L61
Schaffner, J., & Mishustin, I. N. 1996, PhRvC, 53, 1416
Schaffner-Bielich, J., & Gal, A. 2000, PhRvC, 62, 034311
Schulze, H.-J., Polls, A., Ramos, A., & Vidaña, I. 2006, PhRvC, 73, 058801
Sedrakian, A., Weber, F., & Li, J. J. 2020, PhRvD, 102, 041301
Sellahewa, R., & Rios, A. 2014, PhRvC, 90, 054327
Shao, G. Y., Colonna, M., Di Toro, M., Liu, Y. X., & Liu, B. 2013, PhRvD, 87, 096012
Shao, G.-Y., & Liu, Y.-X. 2010, PhRvC, 82, 055801
Shen, H. 2002, PhRvC, 65, 035802
Shen, H., Toki, H., Oyamatsu, K., & Sumiyoshi, K. 2011, ApJS, 197, 20
Shen, Y.-S., & Ren, Z.-Z. 1999, CoTPh, 31, 153
Stergioulas, N., & Friedman, J. L. 1995, ApJ, 444, 306
Stone, J., & Reinhard, P.-G. 2007, PrPNP, 58, 587
Sun, T.-T., Zhang, S.-S., Zhang, Q.-L., & Xia, C.-J. 2019, PhRvD, 99, 023004
Taninah, A., Agbemava, S., Afanasjev, A., & Ring, P. 2020, NuPhB, 800, 135065
Tews, I., Carlson, J., Gandolfi, S., & Reddy, S. 2018, ApJ, 860, 149
Thapa, V. B., Kumar, A., & Sinha, M. 2021a, MNRAS, 507, 2991
Thapa, V. B., & Sinha, M. 2020, PhRvD, 102, 123007
Thapa, V. B., Sinha, M., Li, J. J., & Sedrakian, A. 2021b, PhRvD, 103, 063004
Tolman, R. C. 1939, Phys. Rev., 55, 364
Tolos, L., Centelles, M., & Ramos, A. 2017, PASA, 34, e065
Tong, H., Zhao, P., & Meng, J. 2020, PhRvC, 101, 035802
Typel, S., & Terrero, D. A. 2020, EPJA, 56, 160
Typel, S., & Wolter, H. 1999, NuPhA, 656, 331
Vidaña, I. 2013, NuPhA, 914, 367
Walecka, J. 1974, Ann. Phys., 83, 491
Wang, S., Zhang, H. F., & Dong, J. M. 2014, PhRvC, 90, 055801
Wang, Y. N., & Shen, H. 2010, PhRvC, 81, 025801
Weber, F., & Glendenning, N. K. 1992, ApJ, 390, 541
Wei, J.-B., Chen, H., Burgio, G. F., & Schulze, H.-J. 2017, PhRvD, 96 043008
Weissenborn, S., Chatterjee, D., & Schaffner-Bielich, J. 2012a, PhRvC, 85, 065802
Weissenborn, S., Chatterjee, D., & Schaffner-Bielich, J. 2012b, NuPhA, 881, 62
Weissenborn, S., Chatterjee, D., & Schaffner-Bielich, J. 2013, NuPhA, 914, 421
Weissenborn, S., Sagert, I., Pagliara, G., Hempel, M., & Schaffner-Bielich, J. 2011, ApJL, 740, L14
Whittenbury, D. L., Carroll, J. D., Thomas, A. W., Tsushima, K., & Stone, J. R. 2014, PhRvC, 89, 065801
Wirth, R., & Roth, R. 2016, PhRvL, 117, 182501
Xia, C.-J., Peng, G.-X., Zhao, E.-G., & Zhou, S.-G. 2016a, PhRvD, 93, 085025
Xia, C.-J., Peng, G.-X., Zhao, E.-G., & Zhou, S.-G. 2016b, Science Bulletin, 61, 172
Xiang, H., & Hua, G. 2003, PhRvC, 67, 038801
Yan, Y. 2019, RAA, 19, 072
Zhang, N.-B., & Li, B.-A. 2020, ApJ, 902, 38
Zhao, X.-F. 2014, Eur. Phys. J. A, 50, 80
Zhao, X.-F. 2015, PhRvC, 92, 055802
Zhao, X.-F., & Jia, H.-Y. 2012, PhRvC, 85, 065806
Zhou, X., Li, A., & Li, B.-A. 2021, ApJ, 910, 62
Zhu, Z.-Y., & Li, A. 2018, PhRvC, 97, 035805
Zhu, Z.-Y., Li, A., Hu, J.-N., & Sagawa, H. 2016, PhRvC, 94, 045803
Zhu, Z.-Y., Li, A., Hu, J.-N., & Shen, H. 2019, PhRvC, 99, 025804
Zhu, Z.-Y., Zhou, E.-P., & Li, A. 2018, ApJ, 862, 98
Zuo, W., Lejeune, A., Lombardo, U., & Mathiot, J. 2002a, Eur. Phys. J. A, 14, 469
Zuo, W., Lejeune, A., Lombardo, U., & Mathiot, J. 2002b, NuPhA, 706, 418